Influence of Non-additive Mixing on Colloidal

Diamond Phase Formation from Patchy Particles

Isabela Quintela Matos^a and Fernando A. Escobedo^a*

^aR. F. Smith School of Chemical and Biomolecular Engineering, Cornell University, Ithaca, New

York, USA

* Email: fe13@cornell.edu

ABSTRACT

Mixtures of nanoparticles (NPs) with hybridizing grafted DNA or DNA-like strands have been

shown to create highly tunable NP-NP interactions, which, if designed to give non-additive

mixing, could lead to a richer self-assembly behavior. While non-additive mixing is known to

result in non-trivial phase behavior in molecular fluids, its effects on colloidal/NP materials have

been much less studied. Such effects are explored here via molecular simulations for a binary

system of tetrahedral patchy NPs, known to self-assemble into the diamond phase. The NPs are

modeled with raised patches that interact through a coarse-grained inter-particle potential

representing DNA hybridization between grafted strands. These patchy NPs were found to

spontaneous nucleated into the diamond phase and that hard-interacting NP cores eliminated the

competition between the diamond and BCC phases at the conditions studied. Our results also

showed that while higher non-additivity had a small effect on phase behavior, they kinetically

1

enhanced the formation of the diamond phase. Such a kinetic enhancement is argued to arise from changes in phase packing densities and how these modulate the interfacial free energy of the crystalline nucleus by favoring high-density motifs in the isotropic phase and larger NP vibrations in the diamond phase.

I. INTRODUCTION

Preferential attractions between components in mixtures of nanoparticles (NPs) are usually realized experimentally and modeled computationally by using the effect of hybridizing DNA or DNA-like strands grafted to the components' cores.¹⁻⁵ While these mixtures are of broad interest to create self-assembled NP materials, this study focuses on mixtures whose NP-NP interactions could be designed to give non-additive mixing, as this is expected to open up access to more complex phases, in analogy to how non-additive mixing in molecular fluids is associated with nontrivial phase behavior such as azeotropes and eutectic systems. At a macroscopic level, nonadditive mixing occurs when the volume of the mixed state is either larger (positive) or smaller (negative) than the sum of the pure components' phase volumes. At a microscopic level, nonadditive mixing can be introduced when, for example, the characteristic length " σ " of contact between two particles A and B differs from the arithmetic average of the characteristic contact lengths for A pairs and B pairs so that $(\sigma_{AB} = (\sigma_{AA} + \sigma_{BB})/2 + \Delta)$, where the parameter $\Delta \neq 0$ introduces non-additivity); i.e., it deviates from the so-called Lorentz's additivity rule for spherical sites. One of the first models developed using this property was the Widom-Rowlinson model for a binary mixture of spheres, 6 which produced fluid-vapor and fluid-fluid transitions when the like species are repulsive and unlike species are non-interacting ($\Delta > 0$). Other relevant studies include the Asakura-Oosawa model⁷ for the depletion effect of polymeric depletants on large colloidal particles. In this model, the polymer coils only exclude volume to the colloids but not to other polymer coils. Similarly, the non-additive Holland model⁸ has been used to describe the chemisorption of gases in the crystal phase.

In NP systems, negative non-additivity has been leveraged in studying the shape of complementary NPs to form lattices with higher packing density. A model with positive non-additivity in colloidal NPs proposed by Kumar and Molinero (KM) was shown to lead to the formation of a wide variety of novel mesophases, including some microsegregated phases typically associated with block copolymers (like the lamellar, gyroid, and hexagonal phases). The KM model combined a positive value of Δ with a preferential cross-interaction attractive energy parameter ($\varepsilon_{AB}/\varepsilon_{AA} > 1$). This combination of a stronger attraction with a longer contact distance for unlike NPs can favor the formation of ordered phases because the grouping of the unlike pairs caused by the stronger potential leads to an excess excluded volume which favors the more compact clustering of like pairs, resulting in microphase segregation.

One way to implement a KM-type of non-additivity is to partially graft the surface of NPs with DNA or DNA-like strains. One such case studied before is NPs with four patches in a tetrahedral geometry so that, unlike uniformly coated NPs, these patchy NPs would tend to bond in tetrahedral coordination. This system can provide a fabrication route for diamond-structured colloidal crystals with highly desirable photonic properties. 11–15 However, the assembly of diamond structures presents both kinetic and thermodynamic challenges, such as non-spontaneous crystallization, formation of clathrate structures, and BCC phases competing with the diamond phase. These issues have led to extensive computer simulations that determined the optimal patch width that favors the nucleation of the diamond phase. More recently, Neophytou et al. used Monte Carlo simulations to show that having a binary system of tetrahedrally bonded NPs favored the

thermodynamics and kinetics of diamond formation.²¹ The non-additivity in both the KM and Neophytou's model is enacted artificially in the mixing rule, i.e., there is no shape anisotropy or any explicitly modeled functionalization on the NPs. Hence, in this work, we wanted to use an explicit model that physically encodes positive non-additivity, to identify the role of non-additivity in forming the diamond phase. We chose spherical NPs with raised grafted patches to explore their phase behavior using molecular dynamics. The patches modeled in this work mimic the preferential inter-species attractions between hybridizing grafted DNA or DNA-like strands of different lengths. Hence, as shown later through potential of mean force (PMF) calculations, the positive non-additivity is physically enacted and controlled by decorating the NP surfaces with raised patches of different heights having a preferential attraction. The protruding patches enhance positive mixing additivity since they increase the volume of the resulting diamond phase relative to that of the pure component phases. We tuned the patch's non-additivity and the softness of the NP cores to explore their effects on the proclivity to form the diamond phase. For this purpose, we designed two inter-particle potentials endowed of non-additive PMFs (a soft-core Model-S and a hard-core Model-H) that are representative of NPs with different core types and with DNA hybridizing patches.

The rest of the paper is organized as follows: Section II describes the interparticle potential models, simulation methods, and order parameters employed in this study; Sec. III contains the main results and associated analysis, and Sec. IV provides the concluding remarks and outlook for future work.

II. THEORY AND COMPUTATIONAL DETAILS

A. Grafted Hard Nanoparticle Model (Model-H)

Based on Lorentz's rule, we first designed a coarse-grained non-additive model for grafted NPs using hard colloidal cores (Model-H). This model, whose potential of mean force (PMF) and patchy geometry are depicted in Fig. 1, was intended to single out the effect of the local nonadditivity on phase behavior. The A-B selectivity (mimicking the effect of hybridization between grafted chains), see Fig. 1 (a), is enacted by the attraction between complementary patches (PAB). Each patch is made of 7 identical Lennard-Jones beads in a closed-packed hexagonal arrangement (see Fig. 2(a) and (b)), where $\sigma_P = 0.2$ and ε_{PAB}/kT , with the latter being one of the parameters varied to map phase behavior. The core-core and core-patch interactions are purely repulsive (enacted through the Lennard Jones potential with a cutoff radius shifted to $2^{1/6}\sigma$). We kept the parameters for these interactions constant: $\sigma_{CAA} = \sigma_{CBB} = 1$, $\sigma_{C-Patch} = 0.6$, $\varepsilon_{CAA} = \varepsilon_{CBB} = 0.6$ $\varepsilon_{C-Patch} = 1$. The NPs are modeled as rigid bodies, and all intramolecular interactions are excluded. The PMF as shown in Fig. 1 (b) captures the orientationally averaged NP-NP free energy at different distances, between two patchy NPs in vacuum. These calculations employed a Monte Carlo sampling that places one of the NPs at random positions and orientations within a distance from a fixed NP, following the protocol of Ref. [22]. Figure S1 in the Supplementary Information shows a typical NP-NP orientation distribution from one such PMF calculation. Due to the stronger energetic complementary patch-patch interaction, the PMF for Model-H shows a preferential contact at a longer distance between the unlike NPs ($\sigma_{AB} = \sigma_{CAA} + \sigma_{P}$) than that of the σ_{AA} of like NPs, which interact through the WCA potential. To tune this parameter, we change the height of the patch beads, where height (H) measures the amount of the patch that protrudes outside the core's surface, see Figure 2(b). H ranged from zero (flat patch) to 0.2 ($\sigma_P = H$). The height of the patch is also directly associated with the preferential contact, i.e., NPs with more protruding

patches (representing longer grafted chains) would have a larger σ_{AB} and non-additivity. The patch coverage angle is fixed at $\theta = 30^{\circ}$, as shown in Figure 2 (b), so that as the patch height increases by moving the patch beads away from the core center, so do the bead-bead distance and patch diameter (i.e., of the circumference that inscribes all the beads in one patch). The patch width adopted was based on previous literature on how the patch width can thermodynamically favor the patch interaction.¹⁹

B. Grafted Soft Nanoparticle Model (Model-S)

To identify possible effects associated with the choice of core design, we introduced softness in our soft model (Model-S) by describing the NP cores through the two-body portion of the Stillinger-Weber potential²³ and made the NP cores to be the same regardless of type. The same soft potential has been used before in the study of non-additive NPs, and shown to aid in the formation of different mesophases.¹⁰ The choice of such a soft potential would approximate a case where the core is loosely grafted with flexible chains (while the patches are densely grafted with longer, stiffer chains). A schematic of Model-S can be seen in Fig. 1 (a). Similar to Model-H, the attraction between unlike patches continues to be of the Lennard-Jones type. All the other interactions are calculated using the repulsive short-range Lennard Jones potential ($r_c = 2^{1/6}\sigma$). The PMF for Model-S is depicted in Figure 1 (b). We kept the parameters for these interaction constant: $\sigma_{CAA} = \sigma_{CBB} = 1$, $\sigma_{C-Patch} = 0.6$, $\varepsilon_{CAA} = \varepsilon_{CBB} = \varepsilon_{C-Patch} = 1$. The geometric arrangement of the patches is the same as those shown in Figure 2.

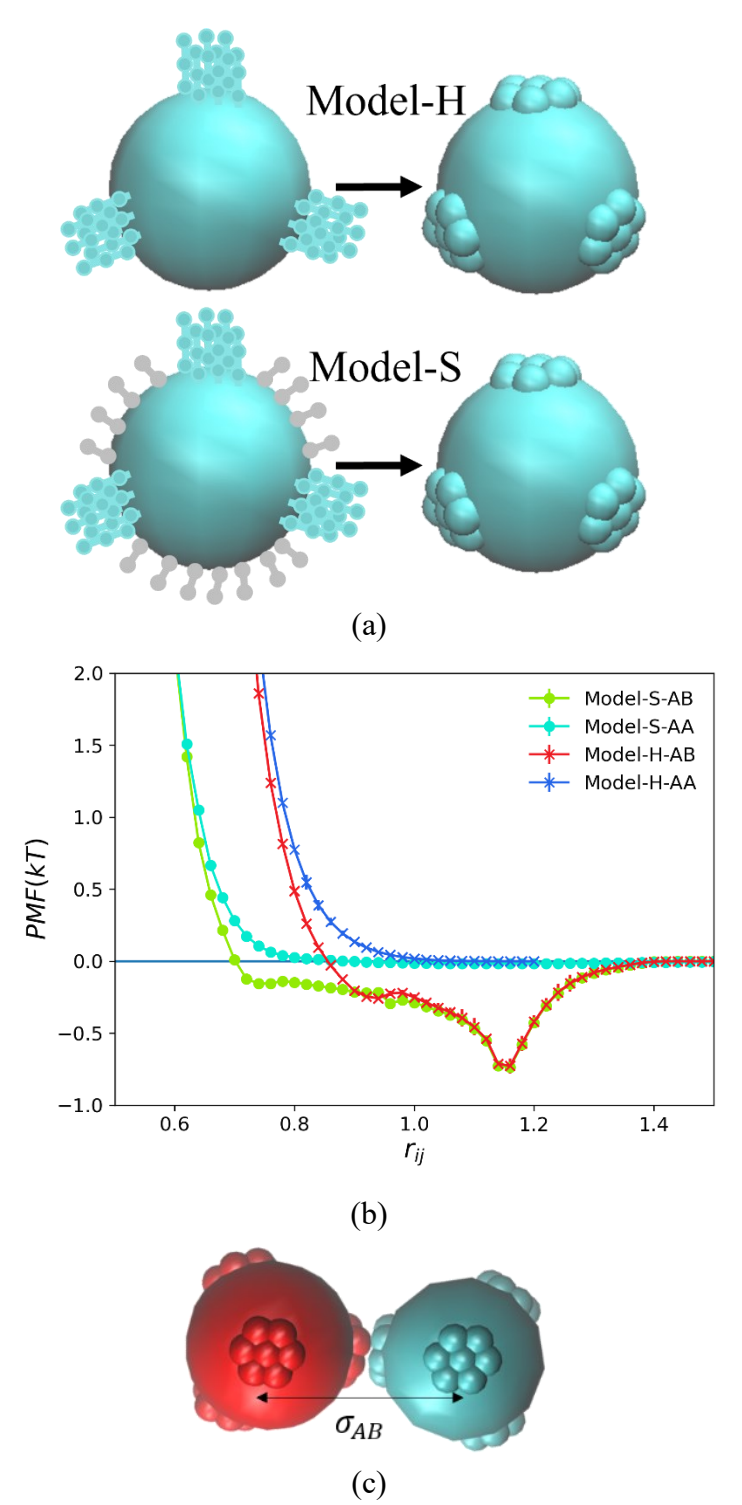


Figure 1. (a) Illustration of the coarse graining of Model-H and Model-S (b) PMF (free energy) between two NPs for Model-H and Model-S in vacuum as a function of their distance r_{ij} . Curves were calculated using $\sigma_{AB} = 1.15$ and $\varepsilon_{PAB}/kT = 0.5$ for both Model-H and Model-S and the PMF values are per particle. (c) Representation of preferential distance between unlike NPs.

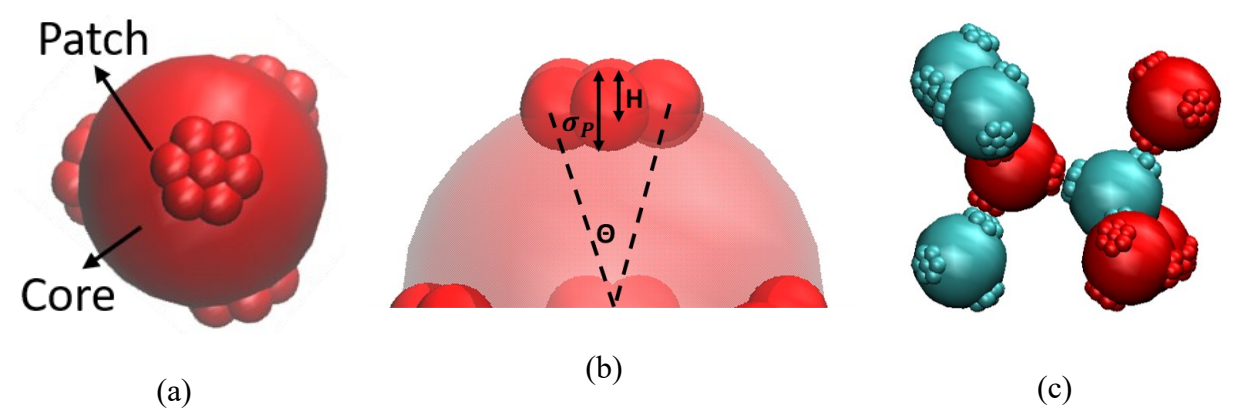


Figure 2. (a) Coarse-grained Model-H having raised patches (as coarse-grained representations of, e.g., complementary DNA grafted on NP surface). The A-B selectivity (hybridization) is modeled using attractive, complementary patches (PA-PB). (b) Patch coverage angle (θ), patch bead diameter (σ_P) and height (H). (c) Unit cell of diamond phase formed with a binary mixture of patchy NPs.

While in the A-B PMF curves of Fig. 1 (b) the main attraction well occurs when the NP patches are aligned as in Fig. 1(c), a secondary shallow well occurs for both models (r_{ij} < 1 for Model-H and r_{ij} < 0.8 for Model-S), associated with the NP patches interacting laterally, as shown in the sample configurations in Fig. S1 (c) and (d) of the Supplementary Information. However, these secondary-well interparticle distances were never observed at the conditions we carried out our bulk many-NP simulations.

C. Simulation details

Molecular dynamic simulations for models H and S were conducted in the isothermal-isobaric (NPT) ensemble with rigid body dynamics and no intramolecular interactions using the LAMMPS software.²⁴ We simulated systems with sizes ranging from N = 512 to 4096 at the equimolar composition to favor the cross-species four-fold coordination expected in a diamond lattice. The initial random configurations were cooled at a rate of 2×10^{-7} kT/step and constant pressure ($P^*=P\sigma^3/\varepsilon=0.5$) from a disordered state ($T^*=kT/\varepsilon=4$) until we observed the formation of an ordered

structure, which occurred for $1 \le T^* \le 0.5$ for Model-H and $2 \le T^* \le 3$ for Model-S. The cooling runs consisted of 3×10^7 steps with a timestep of $\Delta t = 0.001$. Thereafter, we equilibrated the system at the phase formation temperature for 10^7 steps. In some cases, we carried additional heating NPT runs followed by cooling runs to minimize the number of morphological defects.

We computed the transition points between BCC or diamond and isotropic phases using interfacial simulations on LAMMPS. We followed the protocol laid out by Pedersen²⁵ to prepare the simulation cells containing the crystal and isotropic phases and to calculate the difference in free energy necessary to determine if the system had converged to the coexistence ε_{PAB}/kT value. We observed the formation of both BCC and diamond phases in a simulations box for some conditions of ε_{PAB}/kT and σ_{AB} when using Model-S. At these points, we performed simulations in a rectangular box with $L_z=2L_x=L_y$ and N=1024 in the NP_ZT ensemble. We cooled the system down to $T^*=3$ and equilibrated the box at this temperature to check if the BCC/diamond phases were still observed.

The binary system of tetrahedrally bonded patches can assemble in two different polytypes, namely, cubic and hexagonal diamonds. We conducted spontaneous nucleation simulations to calculate the fractions of polytypes, following a methodology similar to that of ref. [21]. Ten independent simulations for six values of σ_{AB} were performed in the NVT ensemble at $T^* = 3$ and number density ($\rho = N\sigma_{AB}/V$) of 0.4. We used the average of the final configurations from those 10 runs to calculate the fraction of NPs in a cubic or hexagonal environment.

The nucleation free-energy barriers for the diamond phase with different patch heights were estimated using the Dual Order Parameter "OP" method.²⁶ A key advantage of this method is that it allows a simple way of implementing biased-sampling (via Umbrella Sampling) over a readily accessible (albeit low quality) OP (λ_1) with molecular dynamics, circumventing the need for

expensive and frequent on-the-fly calculations of a complex (albeit high quality) OP (λ_2), which in this case would track the nucleation of the diamond structure. This method is suitable for low-to-medium degrees of supersaturation, i.e., when the disorder-to-order transition barriers are large enough that no timely spontaneous transition occurs, and a biasing potential on a suitable OP is needed. The Dual OP method assumes that the two OPs (λ_1 and λ_2)are correlated and can be used to track the phase transition.

Following this procedure, we first calculate the free energy as a function of the cheaper OP (λ_1) , i.e., $\beta f(\lambda_1)$, using biasing potentials on λ_1 . Later, we calculated the free energy as a function of the expensive, high-quality OP (λ_2) by using Bayes theorem on data collected during the simulation:

$$\beta f(\lambda_2) = -\ln \sum_{\lambda_1} \Pi(\lambda_1 | \lambda_2) e^{-\beta f(\lambda_1)}$$
(1)

Where $\beta=1/kT$. The parameter λ_1 was chosen to be the potential energy of the system and $\beta f(\lambda_1)$ was obtained using umbrella sampling (US) simulations. The potential energies were pinned with biasing harmonic potential using PLUMED^{27,28} on LAMMPS. The different windows from the US simulations were then unbiased, and the multistate Bennett acceptance ratio (MBAR) method was used to estimate the free energies.²⁹ More details about the US simulations are available in the Supplementary Material. These US simulations were carried out in the NPT ensemble for a system of 4096 NPs at $P^*=0.5$. The temperatures were set relative to the diamondisotropic transition temperature (obtained via interfacial pinning simulations as described before) to target a preset degree of supersaturation ($\beta \mu_D - \beta \mu_I = -2$). This degree of supersaturation was obtained by finding the difference between the chemical potential at the coexistence temperature (β_{coex}) and supersaturation temperature (β_{ss}) for both the isotropic and diamond phases:

$$\beta_{ss}\mu_{D}(\beta_{ss}, P) - \beta_{coex}\mu_{D}(\beta_{coex}, P) = -\int_{T_{coex}}^{T_{ss}} \frac{H_{D}(T)}{NkT^{2}} dT$$

$$\beta_{ss}\mu_{D} - \beta_{ss}\mu_{I} = -\int_{T_{coex}}^{T_{ss}} \frac{H_{D}(T)}{NkT^{2}} dT + \int_{T_{coex}}^{T_{ss}} \frac{H_{I}(T)}{NkT^{2}} dT$$
(2)

where $H_X(T)$ is the configurational enthalpy of phase X evaluated at temperature T. Equation 2 was evaluated using the trapezoidal rule for the numerical integration. The values for the integrands were obtained from NPT simulations of the two phases. The λ_2 OP was defined as the largest cluster of crystal-like NPs and calculated as a post-processing step together with $\beta f(\lambda_2)$. We obtained the error bars for the free energy values with λ_1 using the MBAR method for error estimation, and then the error bars for $\beta f(\lambda_2)$ by applying the errors from MBAR onto Eq. 1.

D. Order parameters

The second OP (λ_2) was chosen to be the largest crystalline cluster. To define the local translational order of a NP, we used the following Steinhardt bond order parameter:³⁰

$$q_{3,m}(i) = \frac{1}{N_B(i)} \sum_{i=1}^{3} Y_{3,m}(\theta_{ij}, \phi_{ij})$$
(3)

where $N_B(i)$ is the number of neighbors of NP i, and $Y_{3,m}(\theta_{ij},\phi_{ij})$ are the spherical harmonics, θ_{ij} and ϕ_{ij} are the polar and azimuthal angles between NP i and its neighbor j. The total angular momentum is set to 3, and the value of m ranges from -3 to 3. The cutoff to define neighbors of NP i is set to $1.4\sigma_{AB}$. We then used the translation correlation parameter $(d_3(i,j))$ between NPs i and j to determine if a NP is in a diamond crystalline environment:

$$d_3(i,j) = \frac{\sum_{m=-3}^3 q_{3,m}(i) q_{3,m}^*(i)}{\left(\sum_{k=-3}^3 \left| q_{3,k}(i) \right|^2\right)^{1/2} \left(\sum_{l=-3}^3 \left| q_{3,l}(j) \right|^2\right)^{1/2}} q_{3,m}(i) \tag{4}$$

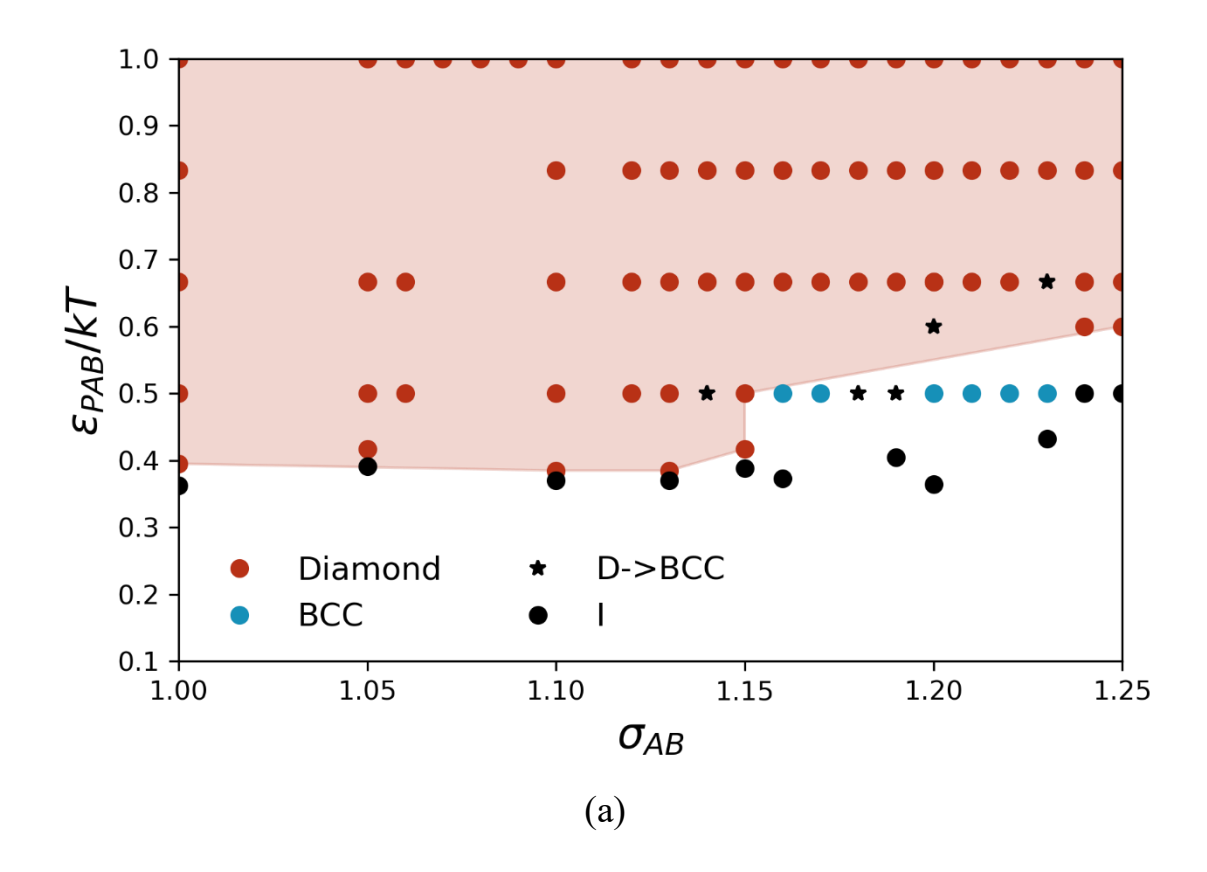
where the asterisk denotes the complex conjugate. We adopted the values of $d_3(i,j)$ established in ref. 20,21 to determine if NPs are crystalline and if they have staggered or eclipsed bonds. According to these references, particles i and j have a staggered bond if $-1 \le d_3(i,j) \le -0.85$ and an eclipsed bond if $-0.3 \le d_3(i,j) \le 0.1$. Particles are crystalline if they have four bonds. The particle is in a cubic environment if four out of four bonds are staggered, while it is in a hexagonal environment if it has one eclipsed and three staggered bonds.

III. RESULTS AND DISCUSSION

A. Influence of NP core-core interactions on the phase diagram

We started our phase exploration of multiple patch cases by grafting two and three patches (with geometry compatible with tetrahedral coordination) with both Model-S and Model-H. However, such minimalistic patchy models did not produce a diamond or other network phase of interest at the studied conditions. Hence, we focus on the four-patch case (i.e., NPs having four tetrahedrally oriented patches on the surface) whose phase diagrams are presented in Figure 3. A video showing the formation of the diamond phase from the isotropic phase is available in the Supplementary Material. We investigated how the height and bonding strength of the raised patches in both Model-S and Model-H influence the formation of such an open lattice as the diamond crystal. The effect of non-additivity and energetic attraction on phase behavior is shown in Figure 3 for both Model-S and Model-H. We also detail in Figure 3 (c) the structure of the diamond phase formed. Since the energetic attractions between patches are only present between unlike NP patches, the energy is minimized in the diamond lattice as this maximizes the number of favorable contacts per NP. The ability of self-assembling diamond phases is observed here over a wide range of the patch height parameter, as indicated by the spontaneous formation of diamond phases for both models investigated. The observed facile self-assembly of the diamond phase corroborated the observation

of a previous study in which the interaction between a binary mixture of flat patches was found to thermodynamically and kinetically favor the diamond phase when compared to a single component system.²¹



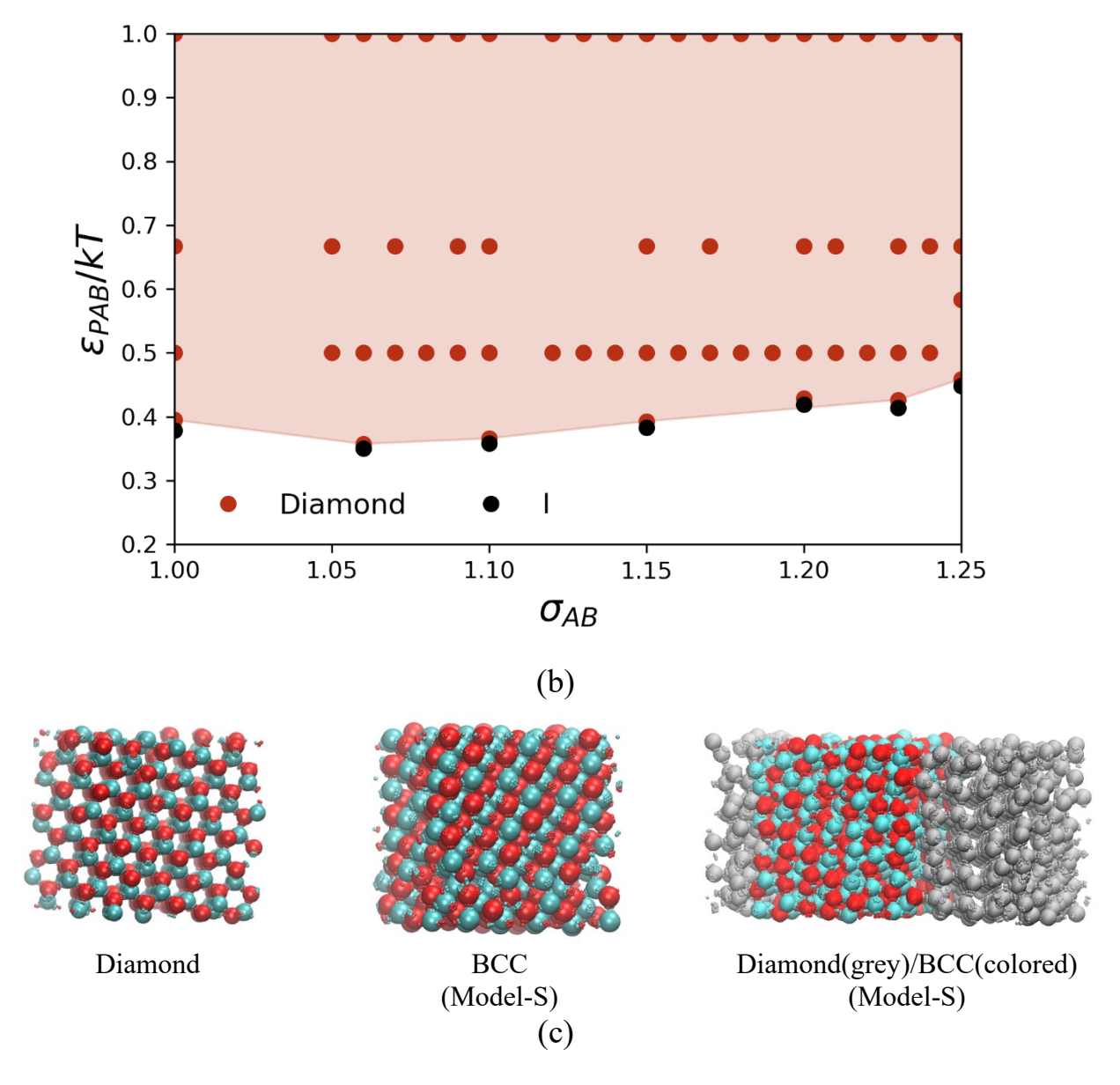


Figure 3. Phase diagrams for the four-patch Model-S (a) and Model-H (b) NP model for an equimolar mixture as a function of the contact distance parameter ratio $(\sigma_{AB}/\sigma_{AA})$ and patch attraction parameter (ε_{PAB}/kT) . Phases obtained using $P^*=0.5$. (c) Representative snapshots of the phases described in (a) and (b).

One of the main characteristics of the diamond crystal is the low packing fraction which would be made even lower by the longer A-B contacts found for NPs with raised patches. Other phases, such as the body-centered cubic (BCC) lattice, may also expectedly compete with the diamond phase for lower values of patch interaction strength. For Model-S, we find conditions where the BCC phase seemed to be in equilibrium with the diamond phase. In fact, for some ε_{PAB}/kT points, we observed that both the BCC and diamond phases were present in the simulation box. Hence, we carried out two-phase interfacial simulations (see simulation details section) to verify if this arrangement could be recreated and maintained; a snapshot of this two-phase coexistence state is shown in Figure 3 (c). The BCC phase formation was not observed for Model-H, which can be attributed to the hard, short-range interaction of unlike cores that do not favor the more numerous core-core contacts prevailing in the BCC phase. Indeed, the softness of core-core interactions allows for closer proximity and hence the more efficient BCC packing in the Model-S cores only. Generally, softer core-core interactions allow for faster equilibration by reducing the kinetic configurational barriers between different structural motifs, but they can also modify the relative thermodynamic stability of competing phases. For example, for a system of additive Janus particles, the softening of the particle cores was implicated in the formation of the diamond phase.³¹ However, we do not see a similar effect of softness for our system, at least in cases where a comparison to such Janus particle system would be reasonable (i.e., for flat patches). The main finding, in terms of core design, is that Model-H should be preferred when targeting the diamond phase for NPs with taller patch heights for the geometry and range of interaction strengths studied. We identified through interfacial simulations the points in which either the diamond or BCC phase melted into the isotropic phase, which are also marked in Fig. 3 for both models. Note that a BCC solid is formed by two interpenetrating diamond lattices, and since the distinct patches are

explicitly modeled in our model, the contacting unlike patches form a network that can be

classified as a double diamond (DD). We calculated structure factors³² to verify the effect of having

explicit patches on the double-diamond/BCC structure (see Figure 4). When we use the center of mass of the NP, the BCC spectrum peak ratios are observed ($\sqrt{2}$: $\sqrt{4}$: $\sqrt{6}$: $\sqrt{8}$: $\sqrt{10}$). Meanwhile, DD peak ratios appear for the calculations with the cores and patches configurations ($\sqrt{2}$: $\sqrt{3}$: $\sqrt{4}$: $\sqrt{6}$: $\sqrt{8}$: $\sqrt{9}$).

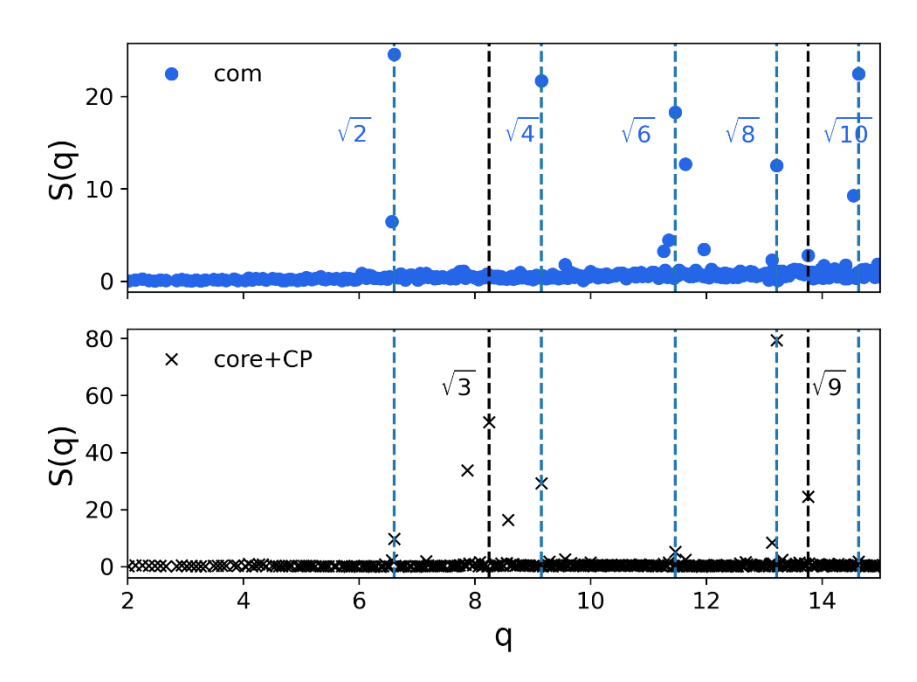


Figure 4. Structure factor calculation considering the coordinates of the center of mass (com) and the individual coordinates of the cores and patches (core+patch) for the double diamond/BCC structure. Simulations for this structure were conducted for Model-S with $\sigma_{AB} = 1.16$ and $\varepsilon_{PAB}/kT = 0.5$.

B. Influence of non-additivity on the Diamond Phase assembly

The diamond phase can be classified as either a cubic or a hexagonal diamond. It is essential to distinguish between the two types because the former has better photonic properties than the latter.¹² Structurally, the cubic diamond phase differentiates from the hexagonal phase by the number of bonds in the staggered configuration. The cubic diamond has all four bonds in the staggered configuration, while the hexagonal diamond has three bonds in the staggered configuration and one bond in the eclipsed configuration.³⁴ Previously, a model for NPs with

implicit tetrahedrally grafted patches was simulated via Monte Carlo simulations to address the influence of the coverage area of the patches on the fractions of hexagonal and cubic-arranged NPs.²¹ They found that wider patches ($\theta > 28^{\circ}$) resulted in a higher relative fraction of cubic diamond. It has also been shown that depletion and DNA-mediated interactions can stabilize the cubic crystal for a narrow parameter region in a system of tetrahedral clusters of NPs.^{11,15} For the following calculations, we used Model-H due to the more extensive range of parameters associated with the diamond phase. We used the correlation parameter ($d_3(i,j)$), to determine if a NP was in a cubic or hexagonal environment. We observe a weak dependence between the relative fraction of cubic diamond and the non-additivity parameter that is directly related to the height of the patch, as seen in Figure 5. The distribution of the d_3 parameter for Figure 5 is given in Fig. S3 of the Supplementary Information. The fractions of hexagonally bonded NPs are slightly larger for σ_{AB} < 1.10, but the fraction plateaus at ~ 50% for taller patches.

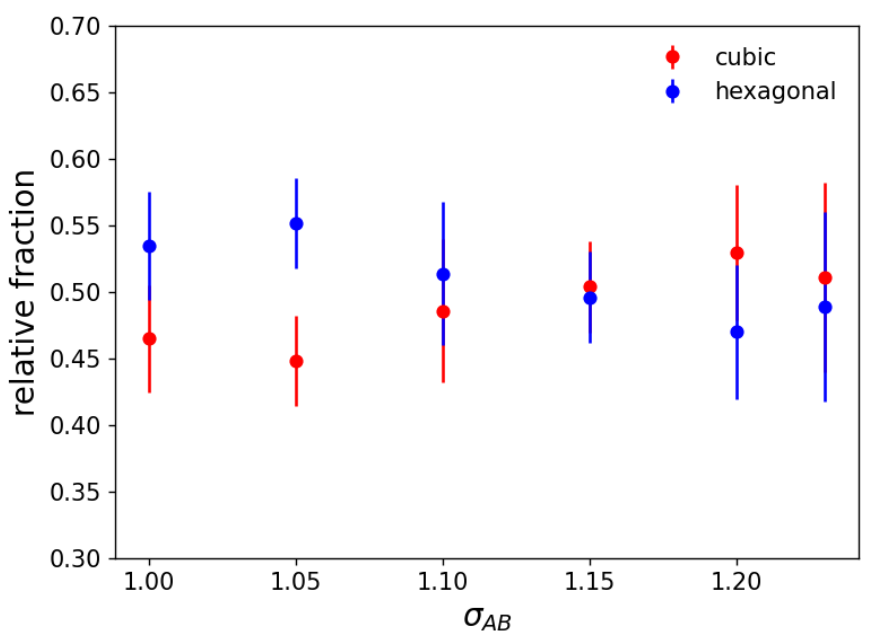
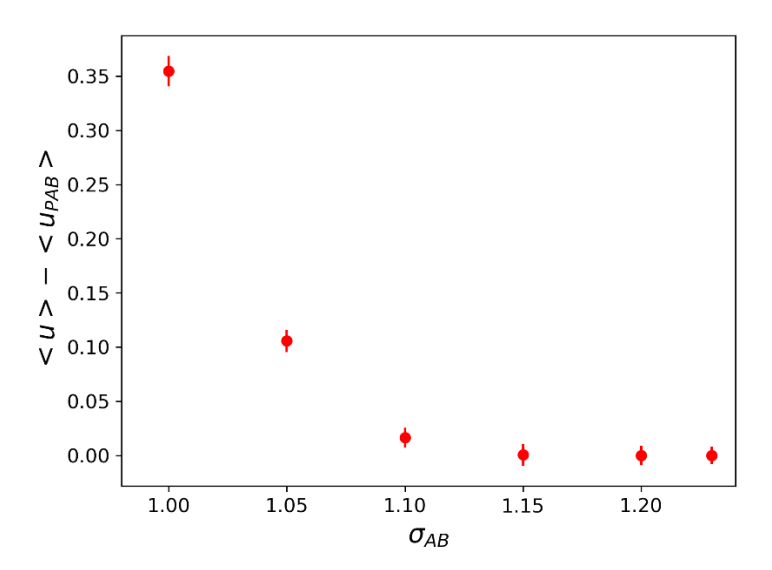


Figure 5. Relative fraction $(N_x/(N_{cubic} + N_{hexagonal}))$ of NPs in cubic and hexagonal environments for different non-additivity parameters (σ_{AB}) following spontaneous nucleation of crystal phase. Simulations were carried out with Model-H, $\varepsilon_{PAB}/kT = 0.5$, and $\rho = 0.4$.

Even though the effect of patch height on the formation of different polytypes was marginal, we noted a difference in the strength of the binding. We ascribe this difference to the flanking effect of having patches of one NP type-A being closer to the core of NP type-B for Model-H when patch height decreases. This flanking effect is evident in Figure 6 (a). If the height of the patch is larger than the cutoff of purely repulsive interactions between patch A and core B, the "bonded" NPs A and B vibrate more around their preferential distance (σ_{AB}) . As a measure of the extent of this vibration, we calculated the mean squared displacements (RMSD) of the NPs forming the diamond phase at T^{coex} for both the flat patch case ($\sigma_{AB}=1$) and three values of σ_{AB} . More details about RMSD calculations are available in the Supplementary Material. The results in Figure 7 show that the NPs with a flat patch vibrate (fluctuate) less than NPs with the taller patches. The vibration of NPs in their respective lattice sites contributes to the NP-entropy through both momenta and configurational degrees of freedom, but the momentum effects are inconsequential in determining phase coexistence conditions as the two phases are in thermal equilibrium. Hence, larger vibration amplitudes of NPs translate into larger vibrational entropy, which would lower the free energy and help stabilize the diamond phase relative to the isotropic phase.



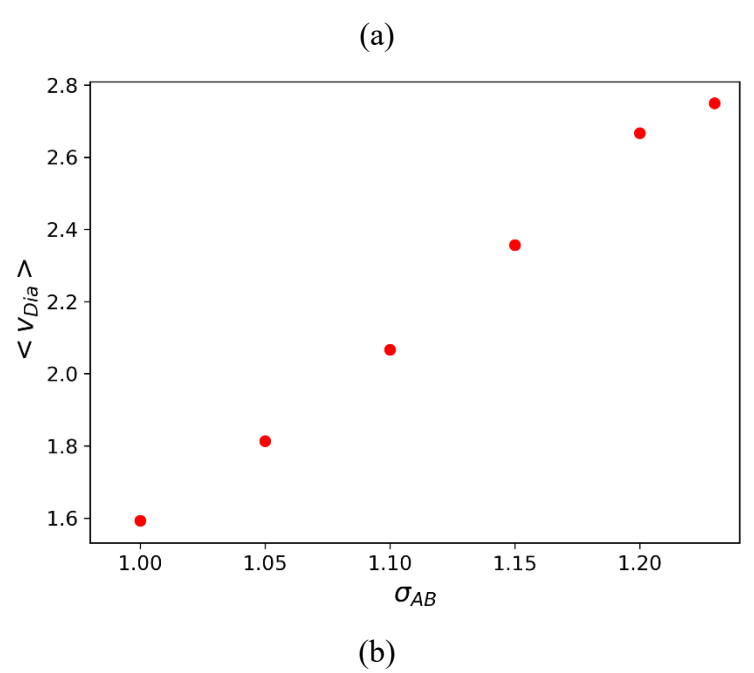


Figure 6. (a) Non-additivity Flanking effect as captured by the average potential energy difference between all interactions ($\langle u \rangle$) and that of unlike patches $\langle u_{PAB} \rangle$). (b) Average molar volume of the diamond phase as a function of the non-additivity parameter. Simulations were carried out for Model-H with $\varepsilon_{PAB} = 1.5$, $P^*=0.5$, and $T=T^{\rm coex}$.

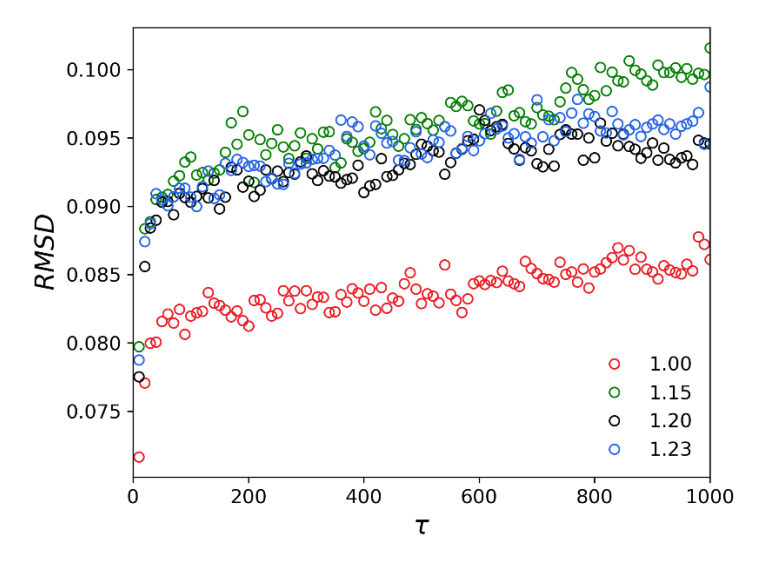


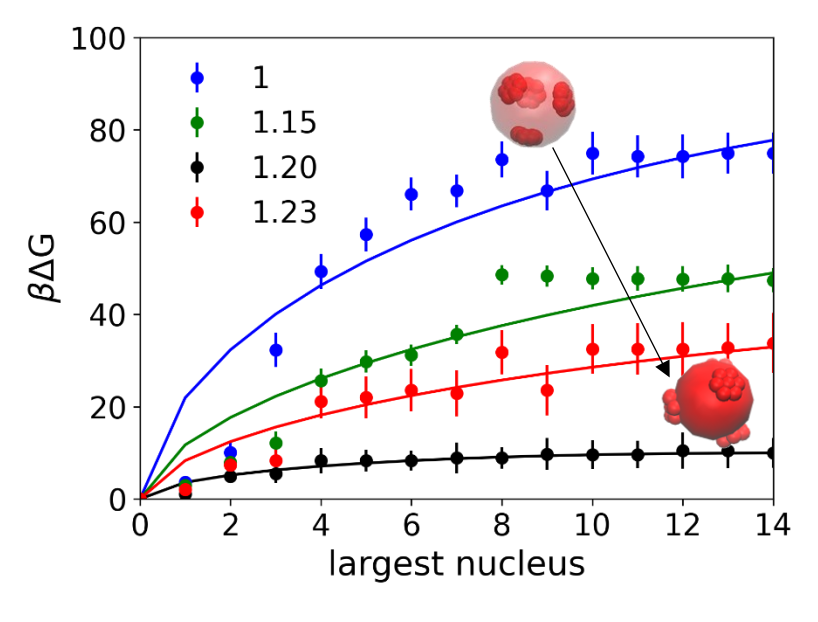
Figure 7. Average Root Mean Squared Displacement (RMSD) of NPs as a function of the simulation time (τ) for four different non-additivity parameters (σ_{AB}) . RMSD was calculated for a defect-free diamond phase at the isotropic-crystal coexistence temperature.

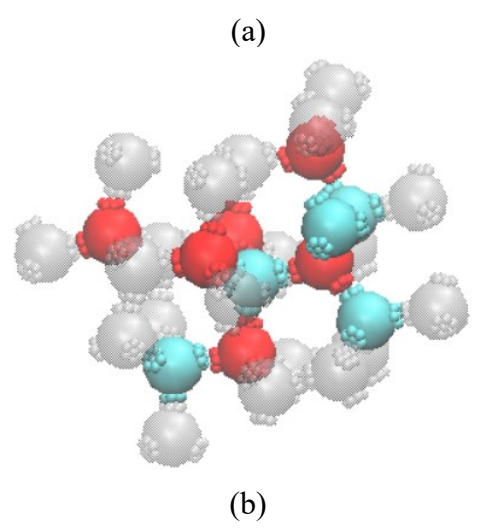
While the stronger energetic bonds of the flat patch favor the diamond structure thermodynamically, as seen by the higher coexistence temperatures, this stronger inter-particle association seemed to slow down the assembly dynamics in our simulations. Indeed, our qualitative observations indicated that, starting from the isotropic phase, the diamond phase (spontaneously) formed significantly more quickly and with fewer defects when the patch height (non-additivity parameter) was larger. The volume of perfect cubic diamond lattice also increased with σ_{AB} , indicating that the channels formed by the open lattice structure are wider for higher σ_{AB} (Figure 6 (b).). We surmised that this extra available volume and the "weaker" binding could help heal defects more readily when nucleating and growing the diamond phase from the isotropic phase. To quantitatively test this conjecture of higher non-additivity correlating with lower diamond-phase nucleation free energy barriers, we calculated these barriers for Model-H for different patch heights. We used umbrella sampling simulations together with the Dual OP method to calculate the needed free energies for three different σ_{AB} values at temperatures corresponding to the same degree of supersaturation ($\beta\Delta\mu$). In this way, all systems being compared experience the same thermodynamic driving force for nucleating the diamond phase. Figure 8 shows the free energy as a function of the number of the largest ordered crystalline cluster (n). We used classical nucleation theory (CNT) to fit the simulation points: assuming a fixed spherical geometry:³⁵

$$\beta \Delta G = -n\beta \Delta \mu + \beta \gamma n^{2/3} \tag{5}$$

where γ is the surface free energy to maintain the crystalline-isotropic interface (which in this expression also absorbs a nucleus-geometry factor ($\beta\gamma A \propto \beta\gamma n^{2/3}$)). The CNT fit, also shown in Figure 8, provides a reasonable correlation to the data trends, albeit deviations are larger for small cluster sizes. The larger barrier size for the flat patch case can be attributed to its higher surface

free energy (whose estimated values are listed in the caption of Fig. 8). We connect this larger interfacial tension to a higher packing density in the crystalline phase and a higher density difference between the isotropic and crystalline phases for the flat patch case when compared to the taller patch cases, as seen in Figure 8 (c). This difference reaches a minimum for $\sigma_{AB} = 1.2$, at which point the volume of the isotropic phase starts to increase, while the volume of the diamond phase plateaus for taller patches. The isotropic phase is always less dense than the diamond phase at phase coexistence, and, at the isotropic phase density maximum ($\sigma_{AB}=1.2$), local fluctuations with the denser diamond coordination motifs are likely better stabilized in the isotropic phase. Evidence of an increase in the AB patch-patch contacts (i.e., a more negative energy) in the isotropic phase for $\sigma_{AB} = 1.2$ is shown in Fig. S2 of the Supplementary Material. This difference in local density can explain why $\sigma_{AB} = 1.2$ has the lowest barrier in Figure 8 (a), indicating an optimal value for the height of the patch. Optimality in terms of patch width has also been observed in flat patch NPs.²⁰ We also note that the $\beta\Delta\mu$ fit from CNT was three times larger than the $\beta\Delta\mu$ calculated with Eq. 2 (i.e., $\beta \Delta \mu$ =2) for the flat patch case (σ_{AB} = 1). Possible causes for such deviations may be related to the effects of structural changes in the nucleus and to a size dependence of the surface energy, which are not accounted for by CNT. Saika-Voivod et al.²⁰, in their study of a single-component flat-patch NPs that assemble into the diamond phase, also found similar discrepancies and showed that $\Delta\mu$ could change by a factor of 2 depending on the order parameter chosen to classify the particles as solid-like.





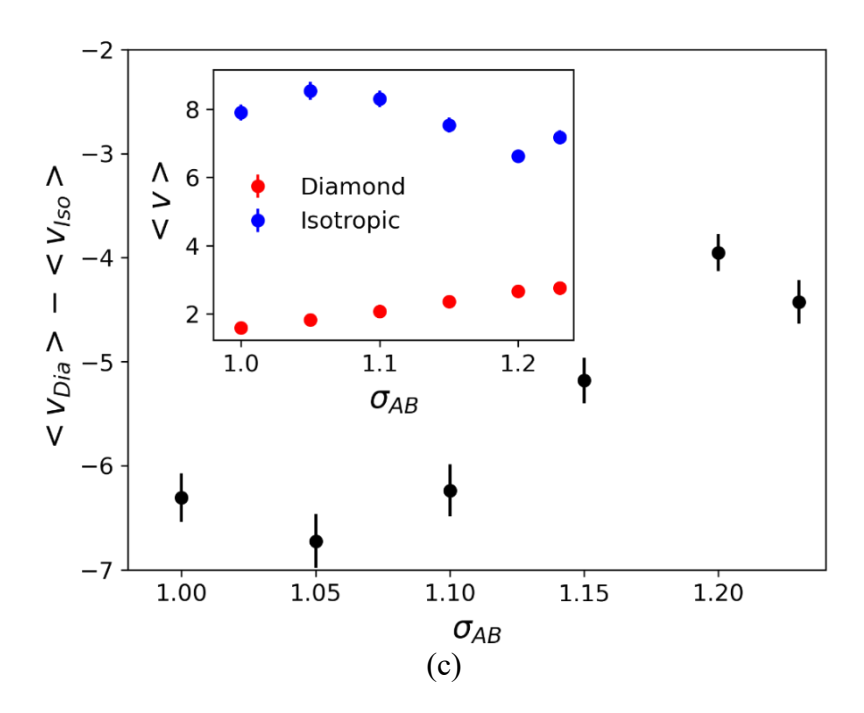


Figure 8. (a) Free energy as a function of the cluster size. Markers correspond to simulation data, and lines correspond to CNT fits with Eq. 5. Fitting parameter values are $\beta\Delta\mu=6.1$ and $\beta\gamma=28.0$ for $\sigma_{AB}=1.00$, $\beta\Delta\mu=2.3$ and $\beta\gamma=14.1$ for $\sigma_{AB}=1.15$, $\beta\Delta\mu=1.3$ and $\beta\gamma=5.0$ for $\sigma_{AB}=1.20$, and $\beta\Delta\mu=1.9$ and $\beta\gamma=10.2$ for $\sigma_{AB}=1.23$. (b) Snapshot of NPs in the nucleus and its vicinity near the critical point (n ~10) for $\sigma_{AB}=1.23$. The crystalline NPs are colored (red and blue). (c) Average molar volume difference between the diamond and isotropic phases as a function of the non-additivity parameter σ_{AB} . Inset shows the average molar volumes for each phase. Simulations were carried out for Model-H with $\sigma_{AA}=1$, $\varepsilon_{PAB}=1.5$, and $\varepsilon_{CAA}=1$.

While we have provided some physical arguments as to why raising the patch height σ_{AB} (relative to the flat-patch case) facilitates the isotropic-diamond transition, this trend reverses for $\sigma_{AB} > 1.2$. This reversal may occur because as patches are made more protruding, the "lateral" patch-patch interactions become more competitive (at least in our model) against the "frontal" patch-patch contacts needed to form the diamond structure. In addition, the density of the diamond phase

decreases as the patch height increases, which, for $\sigma_{AB} > 1.2$, can create a packing entropic cost that is not compensated by the energetic attraction between patches.

IV. CONCLUSIONS

In summary, we explored the phase behavior of A+B binary mixtures of spherical NPs decorated with tetrahedrally arranged patches. These NPs have preferential inter-species attractions to mimic hybridization between grafted DNA or DNA-like strands. The patches are raised to introduce a local, positive non-additive behavior, whose effect on phase and kinetic behavior was explored through molecular simulations. We further used two models, a hard-core model (Model-H) and a soft-core model (Model-S) to investigate the role of NP core softness on the assembly. We found that an equimolar mixture of Model-S NPs can form either the single cubic diamond or the BCC phase depending on patch height and patch-patch attraction strength, whereas Model-H NPs only formed the single diamond phase. The softness of the core facilitates core-core contacts, which makes the BCC phase to be more thermodynamically favored for lower binding strengths between complementary raised patches.

We assessed the influence of the non-additivity parameter on the formation of the diamond phase polytype and crystal nucleation in Model-H only. The largest fraction of cubic diamond was found for a non-additive parameter of $\sigma_{AB} = 1.2$ albeit error bars do not allow a firm conclusion. Overall, we found that non-additivity did not significantly influence the fraction of cubic or hexagonal diamonds, at least for the chosen patch width. Additionally, zero non-additivity (i.e., NPs with flat patches) resulted in stronger binding between patches, which slightly favored the diamond crystal thermodynamically, as seen by the slightly higher isotropic-crystal coexistence temperatures than

those for systems with higher non-additivity. Nonetheless, the non-additivity had a more substantial effect on the nucleation free-energy barriers, with the flat patch case having the highest barrier. This shows that even though non-additivity was not necessary for diamond phase assembly, it helped its formation kinetically. We showed that the non-additivity lowers the difference in molar volume at the interface between the crystalline diamond and isotropic phase, with the smallest density difference and nucleation barrier found for a non-additivity parameter σ_{AB} of 1.2. Macroscopically, this smaller density difference at the interface can be associated with a lower interfacial free energy, whose values were estimated via fits of simulation data to classical nucleation theory. Microscopically, the lower interfacial tension for taller patches can be associated with: (i) a higher isotropic phase density, which is more conducive to stabilize the higher NP-NP bond coordination associated with the diamond phase, and (ii) a slight increase in the NP mobility and vibrational entropy in the diamond phase. Altogether, our results suggest that nonadditivity and the implied length of DNA strains grafted on the NP as patches is an important knob in controlling the formation of the diamond phase. Indeed, toward the formation of open lattices with patchy NPs, whereas patch width has been shown to beneficially modulate NP rotational entropy,³³ our model shows that *patch height* can be used to modulate NP vibrational entropy.

The observed effects of patchy-NP design parameters on the diamond phase could be amplified for other conditions, e.g., for wider patches, for different geometric arrangements of the beads forming the patches, or for NP cores of different sizes and shapes. Besides amplification, other open lattice phases may be accessible by changing the cited parameters. From the observation that non-additivity can increase the local vibrations of NPs in the diamond lattice, patches could be designed to enhance such fluctuations; this would translate into a higher entropy (and lower free energy) and hence an increased stability of the diamond phase. Several aspects of the models

employed here could also be improved to better capture realistic features of our systems. For instance, the coarse-grained patch-patch selective interactions in our model are described by Lennard-Jones type of potentials between the small patch beads across different NPs; a more refined coarse-grained potential could be extracted from PMFs of two NPs where patches contain explicitly modeled DNA strands. Such more refined potentials could alter the way how, e.g., patch-patch bonds align and fluctuate, hence affecting the kinetics and thermodynamics of different diamond polytypes. Finally, while in our study we computed nucleation free-energy barriers and used them as surrogates for nucleation kinetics (in view of their dominant role in the context of, e.g., classical nucleation theory), a more complete kinetic analysis (to quantify rates and transition states) can be performed by using specialized methods that sample transition pathways.^{26,36}

Supporting Information

See the supplementary material for additional details provided pertaining to:

(S1) Orientation distribution from PMF calculations, (S2) Average potential energy of unlike patches ($\langle u_{PAB} \rangle$) for isotropic and diamond phases at coexistence. (S3) Distribution of order parameters for cubic or hexagonal environment classification (S4) Umbrella Sampling calculations, and (S5) RMSD calculations. (Supporting Information for Publication.docx)

Video of the formation of the diamond phase from the isotropic phase (diamond phase formation.mpg)

Corresponding Author

*Fernando A. Escobedo – R. F. Smith School of Chemical and Biomolecular Engineering, Cornell University, Ithaca, New York, USA; Email: fe13@cornell.edu

ACKNOWLEDGMENTS

Funding support from NSF Awards No. CBET-1907369 and CHE-2101829 is gratefully acknowledged. I.Q.M. gratefully acknowledges Drs. Ankita J. Mukhtyar and Abhishek K. Sharma for fruitful discussion and the support from the 2021 MolSSI Fellowship.

REFERENCES

- (1) Whitfield, C. J.; Zhang, M.; Winterwerber, P.; Wu, Y.; Ng, D. Y. W.; Weil, T. Functional DNA-Polymer Conjugates. *Chem. Rev.* **2021**, *121* (18), 11030–11084. https://doi.org/10.1021/acs.chemrev.0c01074.
- (2) Boles, M. A.; Engel, M.; Talapin, D. V. Self-Assembly of Colloidal Nanocrystals: From Intricate Structures to Functional Materials. *Chem. Rev.* **2016**, *116* (*18*), 11220–11289. https://doi.org/10.1021/acs.chemrev.6b00196.
- (3) Rogers, W. B.; Shih, W. M.; Manoharan, V. N. Using DNA to Program the Self-Assembly of Colloidal Nanoparticles and Microparticles. *Na.t Rev. Mater.* **2016**, *I* (3), 1–14. https://doi.org/10.1038/natrevmats.2016.8.
- (4) Wang, S.; Xie, X.; Chen, Z.; Ma, N.; Zhang, X.; Li, K.; Teng, C.; Ke, Y.; Tian, Y. DNA-Grafted 3D Superlattice Self-Assembly. *Int. J. Mol. Sci.* 2021, 22 (14), 7558. https://doi.org/10.3390/IJMS22147558.
- (5) Knorowski, C.; Travesset, A. Self-Assembly and Crystallization of Hairy (*f*-Star) and DNA-Grafted Nanocubes. *J. Am. Chem. Soc.* **2014**, *136* (2), 653–659. https://doi.org/10.1021/ja406241n.
- (6) Widom, B.; Rowlinson, J. S. New Model for the Study of Liquid-Vapor Phase Transitions. *J Chem. Phys.* **1970**, *52* (4), 1670–1684. https://doi.org/10.1063/1.1673203.
- (7) Asakura, S.; Oosawa, F. On Interaction between Two Bodies Immersed in a Solution of Macromolecules. *J. Chem. Phys.* **1954**, 22, 1255. https://doi.org/10.1063/1.1740347.

- (8) Holland, B. W. Mixed Localized-Unlocalized Adsorbed Monolayers: Part 2. The Collision Frequency. *Transactions of the Faraday Society* **1965**, *61*, 555–557. https://doi.org/10.1039/TF9656100555.
- (9) Quintela Matos, I.; Escobedo, F. Congruent Phase Behavior of a Binary Compound Crystal of Colloidal Spheres and Dimpled Cubes. *J. Chem. Phys.* **2020**, *153* (21), 214503. https://doi.org/10.1063/5.0030174.
- (10) Kumar, A.; Molinero, V. Self-Assembly of Mesophases from Nanoparticles. *J. Phys. Chem. Lett.* **2017**, *8* (20), 5053–5058. https://doi.org/10.1021/acs.jpclett.7b02237.
- (11) He, M.; Gales, J. P.; Ducrot, É.; Gong, Z.; Yi, G.-R.; Sacanna, S.; Pine, D. J. Colloidal Diamond. *Nature* **2020**, *585* (7826), 524–529. https://doi.org/10.1038/s41586-020-2718-6.
- (12) Neophytou, A.; Manoharan, V. N.; Chakrabarti, D. Self-Assembly of Patchy Colloidal Rods into Photonic Crystals Robust to Stacking Faults. *ACS Nano* **2021**, *15* (2), 2668–2678. https://pubs.acs.org/doi/10.1021/acsnano.0c07824.
- (13) Ho, K. M.; Chan, C. T.; Soukoulis, C. M. Existence of a Photonic Gap in Periodic Dielectric Structures. *Phys. Rev. Lett.* **1990**, *65* (25), 3152. https://doi.org/10.1103/PhysRevLett.65.3152.
- (14) Maldovan, M.; Thomas, E. L. Diamond-Structured Photonic Crystals. *Nat. Mater.* **2004**, *3* (9), 593–600. https://doi.org/10.1038/nmat1201.
- (15) Marín-Aguilar, S.; Camerin, F.; Dijkstra, M. Guiding the Self-Assembly of Colloidal Diamond. *J. Chem. Phys.* **2022**, *157* (15), 154503. https://doi.org/10.1063/5.0109377.
- (16) Sciortino, F.; Giacometti, A.; Pastore, G. Phase Diagram of Janus Particles. *Phys. Rev. Lett.* **2009**, *103* (23), 237801. https://doi.org/10.1103/PhysRevLett.103.237801.
- Zdeněk Preisler; Teun Vissers; Gianmarco Munaò; Frank Smallenburg; Francesco Sciortino.
 Equilibrium Phases of One-Patch Colloids with Short-Range Attractions. *Soft Matter* 2014, *10* (28), 5121–5128. https://doi.org/10.1039/C4SM00505H.
- (18) Noya, E. G.; Vega, C.; Doye, J. P. K.; Louis, A. A. The Stability of a Crystal with Diamond Structure for Patchy Particles with Tetrahedral Symmetry. *J. Chem. Phys.* **2010**, *132* (23), 234511. https://doi.org/10.1063/1.3454907.
- (19) Romano, F.; Sciortino, F. Patterning Symmetry in the Rational Design of Colloidal Crystals. *Nat. Commun.* **2012**, *3* (1), 1–6. https://doi.org/10.1038/ncomms1968.
- (20) Saika-Voivod, I.; Romano, F.; Sciortino, F. Nucleation Barriers in Tetrahedral Liquids Spanning Glassy and Crystallizing Regimes. *J. Chem. Phys.* **2011**, *135* (12), 124506. https://doi.org/10.1063/1.3638046.
- (21) Neophytou, A.; Chakrabarti, D.; Sciortino, F. Facile Self-Assembly of Colloidal Diamond from Tetrahedral Patchy Particles via Ring Selection. *PNAS.* **2021**, *118* (48) e2109776118. https://doi.org/10.1073/pnas.2109776118.
- (22) Agarwal, U.; Escobedo, F. A. Mesophase Behaviour of Polyhedral Particles. *Nat. Mater.* **2011**, *10* (3), 230–235. https://doi.org/10.1038/nmat2959.

- (23) Stillinger, F. H.; Weber, T. A. Computer Simulation of Local Order in Condensed Phases of Silicon. *Phys. Rev. B.* **1985**, *31* (8), 5262. https://doi.org/10.1103/PhysRevB.31.5262.
- (24) Thompson, A. P.; Aktulga, H. M.; Berger, R.; Bolintineanu, D. S.; Brown, W. M.; Crozier, P. S.; in 't Veld, P. J.; Kohlmeyer, A.; Moore, S. G.; Nguyen, et al. LAMMPS a Flexible Simulation Tool for Particle-Based Materials Modeling at the Atomic, Meso, and Continuum Scales. *Comput. Phys. Commun.* **2022**, *271*, 108171. https://doi.org/10.1016/J.CPC.2021.108171.
- (25) Pedersen, U. R. Direct Calculation of the Solid-Liquid Gibbs Free Energy Difference in a Single Equilibrium Simulation. *J. Chem. Phys.* **2013**, *139* (10), 104102. https://doi.org/10.1063/1.4818747.
- (26) Meadley, S. L.; Escobedo, F. A. Thermodynamics and Kinetics of Bubble Nucleation: Simulation Methodology. *J Chem. Phys.* **2012**, *137* (7), 074109. https://doi.org/10.1063/1.4745082.
- (27) Bonomi, M.; Branduardi, D.; Bussi, G.; Camilloni, C.; Provasi, D.; Raiteri, P.; Donadio, D.; Marinelli, F.; Pietrucci, F.; Broglia, et al. M. PLUMED: A Portable Plugin for Free-Energy Calculations with Molecular Dynamics. *Comput. Phys. Commun.* **2009**, *180* (10), 1961–1972. https://doi.org/10.1016/J.CPC.2009.05.011.
- (28) Tribello, G. A.; Bonomi, M.; Branduardi, D.; Camilloni, C.; Bussi, G. PLUMED 2: New Feathers for an Old Bird. *Comput. Phys. Commun.* **2014**, *185* (2), 604–613. https://doi.org/10.1016/J.CPC.2013.09.018.
- (29) Shirts, M. R.; Chodera, J. D. Statistically Optimal Analysis of Samples from Multiple Equilibrium States. *J. Chem. Phys.* **2008**, *129* (12), 124105. https://doi.org/10.1063/1.2978177.
- (30) Steinhardt, P. J.; Nelson, D. R.; Ronchetti, M. Bond-Orientational Order in Liquids and Glasses. *Phys. Rev. B* **1983**, 28 (2), 784. https://doi.org/10.1103/PhysRevB.28.784.
- (31) Li, Z. W.; Sun, Y. W.; Wang, Y. H.; Zhu, Y. L.; Lu, Z. Y.; Sun, Z. Y. Softness-Enhanced Self-Assembly of Pyrochlore- And Perovskite-like Colloidal Photonic Crystals from Triblock Janus Particles. *J. Phys. Chem. Lett.* **2021**, *12* (30), 7159–7165. https://doi.org/10.1021/acs.jpclett.1c01969.
- (32) Schultz, A. J.; Hall, C. K.; Genzer, J. Obtaining Concentration Profiles from Computer Simulation Structure Factors. *Macromolecules* **2007**, *40* (8), 2629–2632. https://doi.org/10.1021/ma062836d.
- (33) Hyde, S. T. Bicontinuous Structures in Lyotropic Liquid Crystals and Crystalline Hyperbolic Surfaces. *Curr. Opin. Solid State Mater. Sci.* **1996**, *I* (5), 653–662. https://doi.org/10.1016/S1359-0286(96)80047-7.
- (34) Romano, F.; Sanz, E.; Sciortino, F. Crystallization of Tetrahedral Patchy Particles in Silico. *J. Chem. Phys.* **2011**, *134* (17), 174502. https://doi.org/10.1063/1.3578182.
- (35) Sharma, A. K.; Escobedo, F. A. Nucleus-Size Pinning for Determination of Nucleation Free-Energy Barriers and Nucleus Geometry. *J. Chem. Phys.* **2018**, *148* (18), 184104. https://doi.org/10.1063/1.5021602.
- (36) Thapar, V.; Escobedo, F. A. Simultaneous Estimation of Free Energies and Rates Using Forward Flux Sampling and Mean First Passage Times. *J. Chem. Phys.* **2015**, *143* (24), 244113. https://doi.org/10.1063/1.4938248.

TOC Graphic

